File S3

S. 1

S.1.1 Statistical distribution characteristics of AEP pre and after earthquakes

Figure S1 presents the global statistical distributions of Anomaly Emphasis Proximity (AEP) values derived from an extensive dataset of seismic events between 2005 and 2020. The AEP data for both LST and SST deviate from a standard normal distribution and exhibit distinct right-skewed, multimodal features with long tails. We applied a Double Gamma mixture model to capture these stochastic properties, and the model achieved a high goodness-of-fit (e.g., $R^2 = 0.990$ for Pre-EQ LST). Establishing a robust baseline is **essential** for defining a "Strong AEP" signal. However, the inherent asymmetry of these distributions limits the utility of the arithmetic mean as an unbiased estimator. The observed "long tail" likely reflects extreme values driven by observational noise or complex surface heterogeneities. This pattern is particularly clear in land systems (Figure S1a), where the observed Mean (4.45) shifts toward the right tail and deviates from both the peak probability density and the Model Expectation (3.88). Such discrepancies indicate that the mean overestimates the central tendency due to its sensitivity to outliers. Even in ocean systems (SST, Figure S1c-d), which are relatively more homogeneous, the right-skewed nature still introduces instability into the mean value.

In contrast to the mean, the median offers superior stability against outliers. Across all panels in Figure S1, the Median (solid red line) aligns closely with the dense "core" of the data distribution, represented by the primary peak of the Gamma fit. This provides a more accurate reflection of the typical background state. In the Pre-EQ LST dataset, for example, the Median (3.80) is nearly identical to the Model Expectation (3.88), which minimizes the bias observed in the mean. Additionally, our extensive regional analysis (as shown in Figure S2-S5) confirms that the median remains statistically stable across different tectonic zones, while the mean fluctuates due to local noise. We therefore adopt the median as the robust baseline to mitigate biases from non-normal distributions and observational errors. We define a "Strong AEP" as any value exceeding this stable median threshold. This ensures that identified anomalies are statistically significant and reflect the physical system’s behavior rather than artifacts of the distribution's tail.

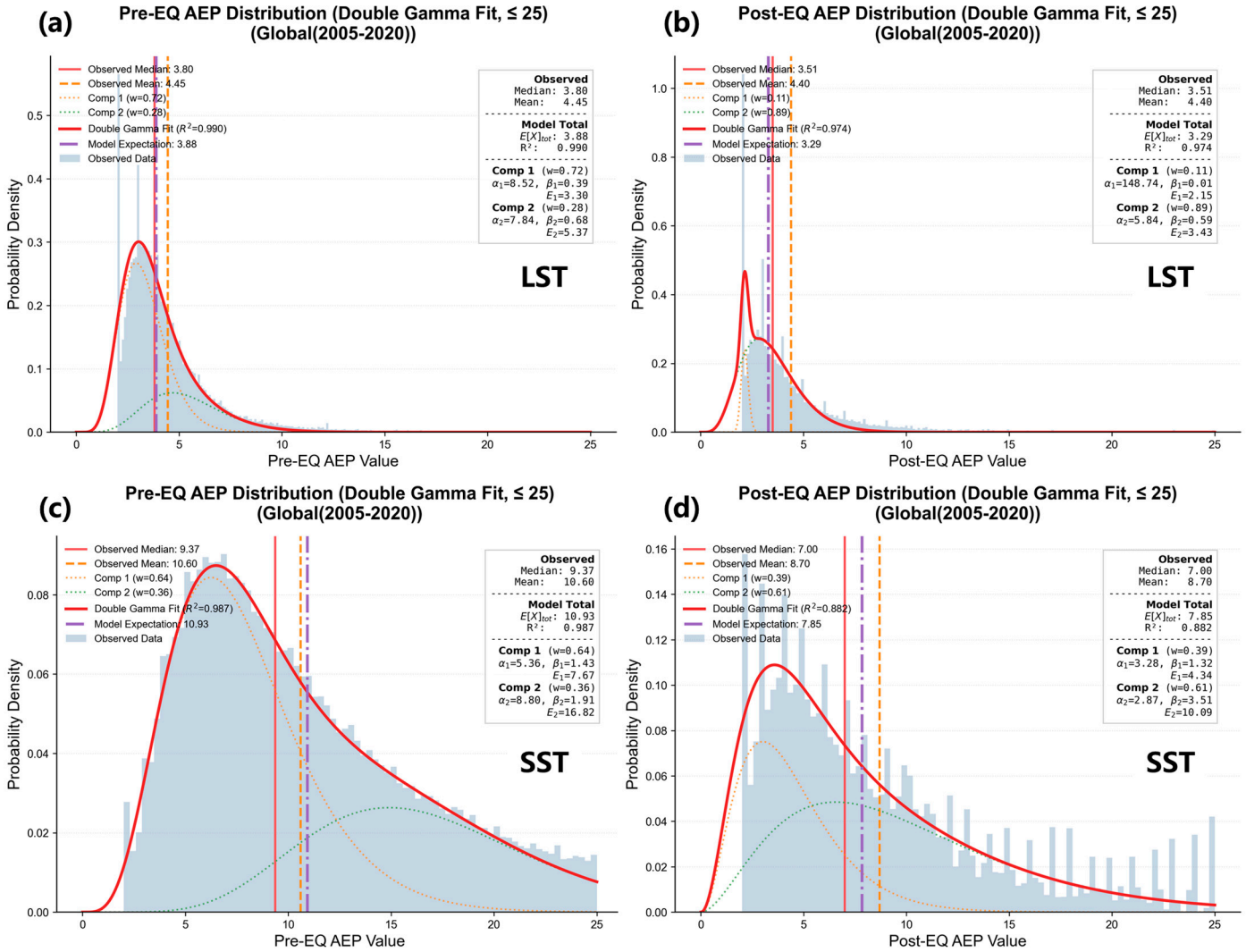


Figure S1 Statistical distributions of Anomaly Emphasis Proximity (AEP) associated with global seismic events (2005–2020). The histograms display the probability density of AEP derived from (a, b) Land Surface Temperature (LST) and (c, d) Sea Surface Temperature (SST) for pre- and post-earthquake periods, respectively. A Double Gamma mixture model (solid red curves) was employed to fit the data due to the observed right-skewed and multimodal characteristics. Vertical lines indicate the observed median (solid red), observed mean (dashed orange), and the model's total expectation (dash-dotted purple).

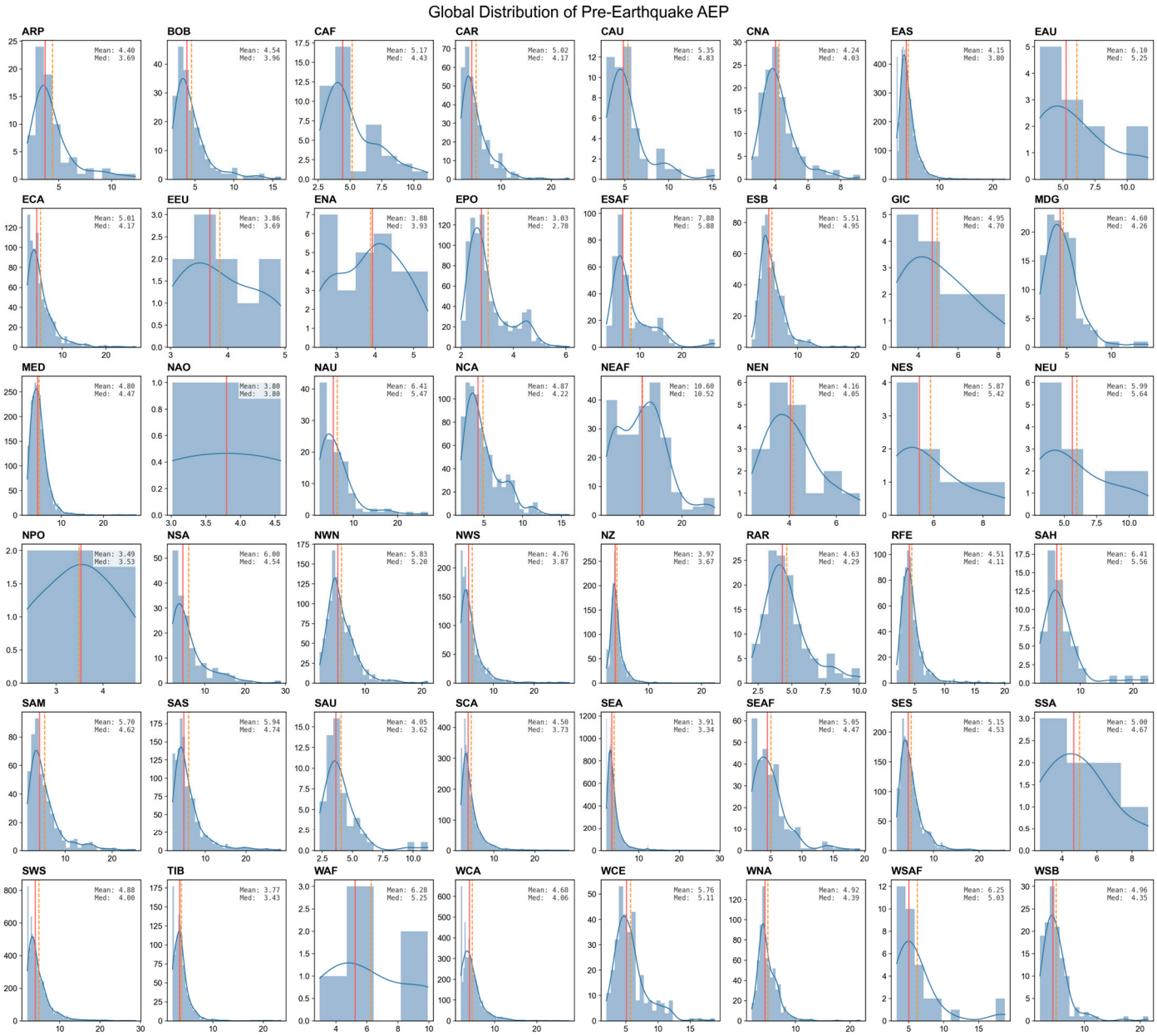


Figure S2 Statistical distributions of AEP values associated with IPCC-AR6 seismic events derived from pre-earthquake LST (2005–2020).

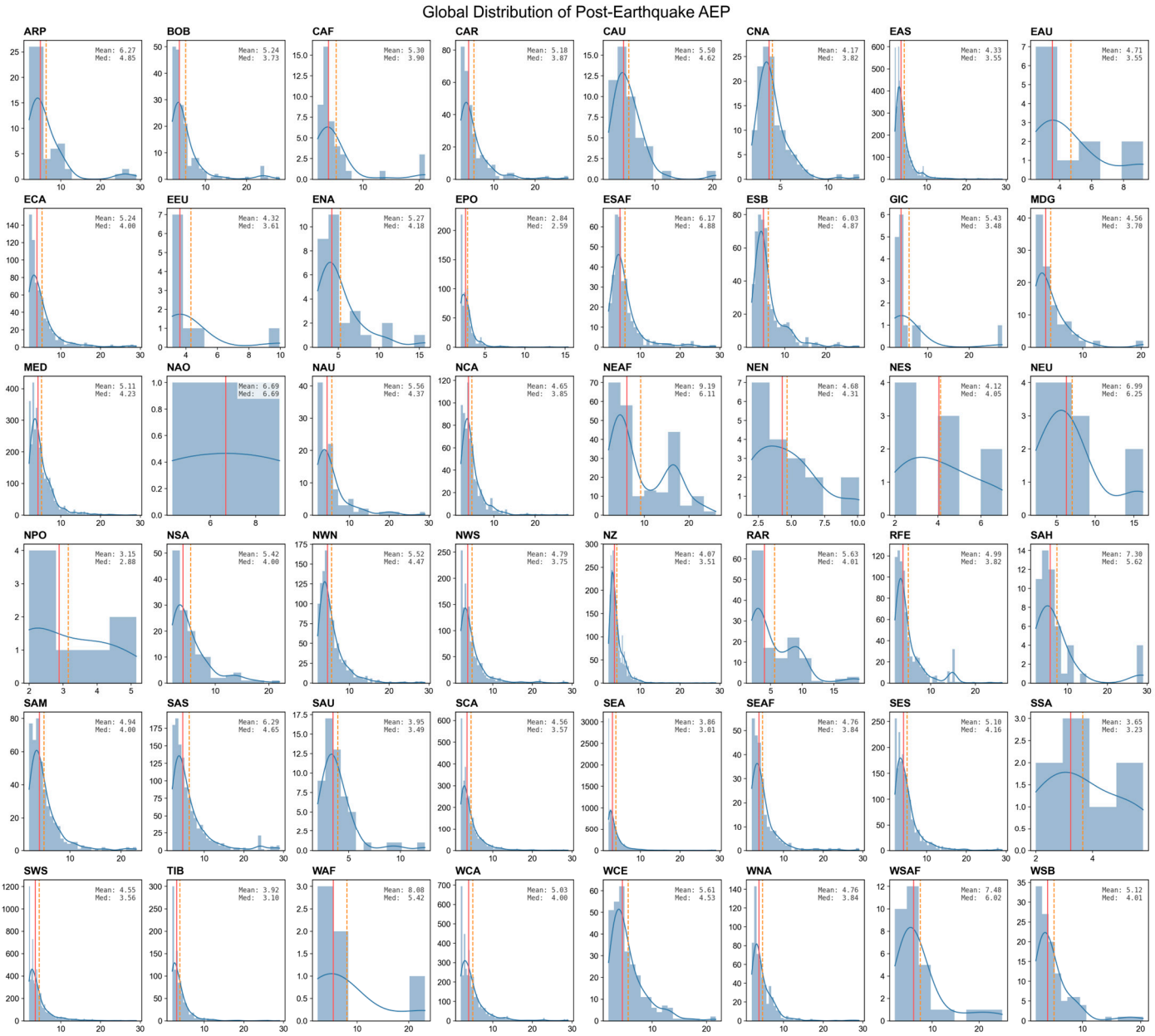


Figure S3 Statistical distributions of AEP values associated with IPCC-AR6 seismic events derived from post-earthquake LST (2005–2020).

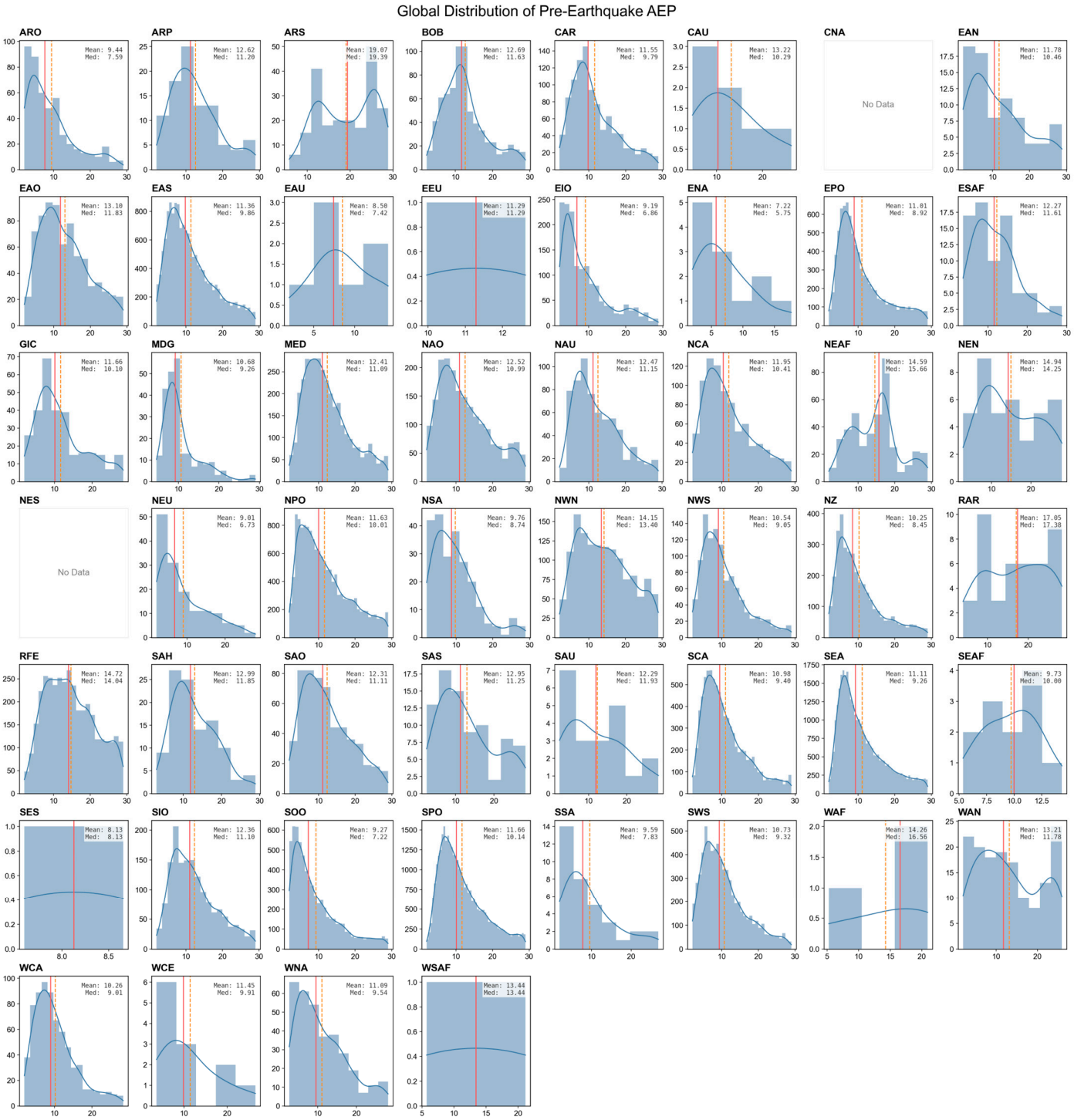


Figure S4 Statistical distributions of AEP values associated with IPCC-AR6 seismic events derived from post-earthquake SST (2005–2020).

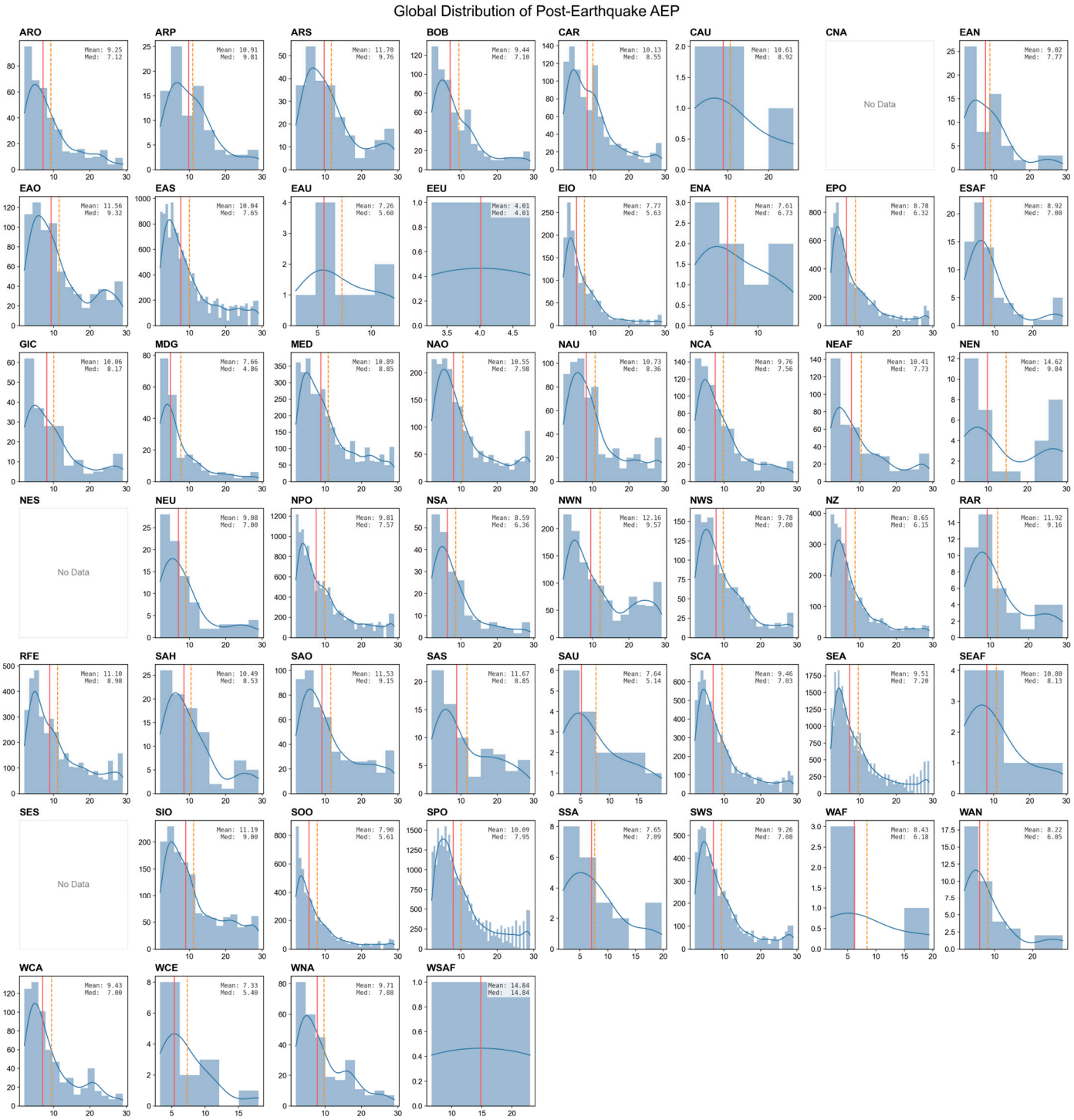


Figure S5 Statistical distributions of AEP values associated with IPCC-AR6 seismic events derived from post-earthquake SST (2005–2020).

S.1.2 Framework of IPCC-AR6 Climate Reference Regions

Global surface temperature fields exhibit significant spatial heterogeneity, governed not only by latitudinal but also by land-sea distribution and atmospheric circulation. To evaluate the spatiotemporal characteristics of pre-earthquake thermal anomalies under a unified geographic framework, this study compared several mainstream climate classification schemes.

The traditional Köppen-Geiger classification, while widely applied in terrestrial climate research, relies primarily on vegetation, temperature, and precipitation characteristics. It lacks coverage of marine areas (comprising only 32 land zones), making it

unsuitable for the Sea Surface Temperature (SST) anomaly analysis required in this study. Similarly, the earlier IPCC AR5 classification, despite introducing regional concepts, lacked sufficient granularity in its division of oceanic regions. In contrast, the latest Reference Regions framework adopted by the IPCC Sixth Assessment Report (AR6-WGI) achieves comprehensive global coverage, as shown in Figure S4. This framework not only optimizes land boundaries to better reflect climatic consistency but, crucially, incorporates 12 major ocean regions. This allows for the parallel analysis of Land Surface Temperature (LST) and Sea Surface Temperature (SST) anomalies within a standardized system.

Consequently, this study adopts the IPCC AR6-WGI framework, which partitions the globe into 58 independent geographic units (consisting of 46 land regions and 12 ocean regions). Based on the principle of "climatic consistency," this scheme considers both geographic proximity and distinct atmospheric circulation features (e.g., monsoon regions, arid zones, and polar circulation). Therefore, utilizing this framework for global regional statistical analysis helps mitigate the confounding effects of background climatic variability (i.e., eliminating interference caused by regional climatic differences).

Notes: Detailed definitions, abbreviation codes, and land/sea attributes for each region are provided in the standard IPCC-AR6 definitions.

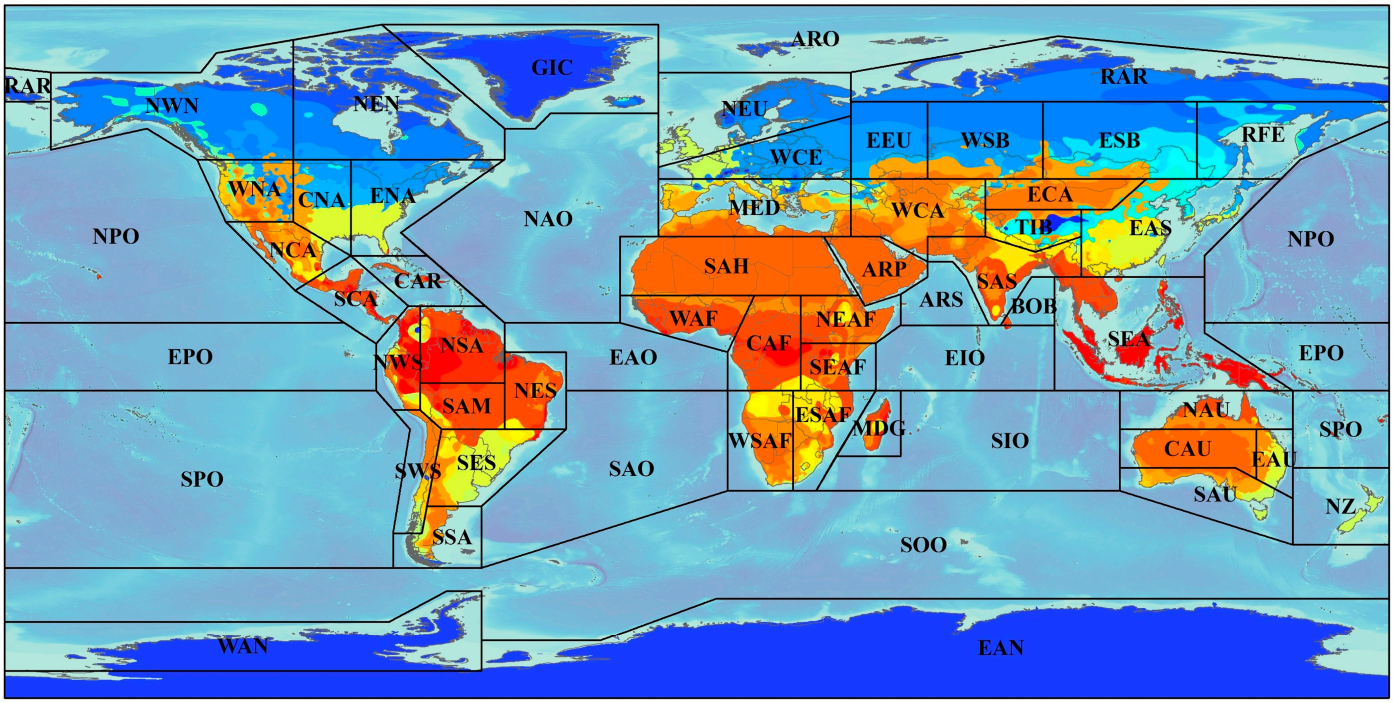


Figure S6 Framework of IPCC-AR6 Climate Reference Regions

S.1.3 Quantification and Classification of Seismically Active Zones

To achieve a refined assessment of global pre-earthquake thermal anomalies, this study employed Kernel Density Estimation (KDE) to quantify and classify the spatial distribution of global seismicity. Utilizing global seismic events with magnitudes $M \geq 4$ from the USGS catalog between January 1, 2000, and December 31, 2020, we calculated the geospatial kernel density field and subsequently delineated seismically active zones (as shown in Figure S7).

First, the global geographic space was discretized into a regular latitude-longitude grid with a resolution of $0.01^\circ \times 0.01^\circ$. For any given grid node (B_x, L_y), the Quartic Kernel Function was employed to estimate the seismic kernel density. The selection of the search radius r followed Silverman's Rule of Thumb, referencing the implementation algorithm in ArcMap 10.8. Specifically, by traversing all seismic events within the search

radius r, the distance from each event to the grid node and its contribution to the density were calculated. The kernel density $D_{(x,y)}$ at that point is expressed as follows:

$$D_{((x,y))} = 1/r^2 \sum (i = 1)^n \left[3/\pi \cdot \mathrm{mag}_i \cdot \left(1 - \left((\mathrm{dist}_i)/r\right)^2\right)^2\right] \quad \text{(S1)}$$

Where n represents the total number of seismic events within the search radius r; mag_i denotes the magnitude of the i-th seismic event; and dist_i represents the geospatial distance between the grid node (B_x, L_y) and the epicenter of the i-th event.

As indicated by Equation, the amplitude of kernel density depends on both earthquake magnitude and spatial clustering. In regions with low seismic frequency, density values are extremely small. To enhance data interpretability and facilitate classification, a base-10 logarithmic transformation was applied to the kernel density results. Empirical estimates suggest that when $\log_{10}(D_{(x,y)}) < -4.5$, seismic activity in the region is negligible (typically corresponding to fewer than two micro-seismic events within a 100 km search radius) and can be treated as background noise to be excluded. Therefore, this study retained only values within the interval $[-4.5, \max(\log_{10} D)]$ and employed the Quartile method to divide this range into four levels, corresponding to Extremely High, High, Moderate, and Low seismicity zones, respectively.

Based on the statistical results calculated from the global seismic data, the specific quantitative thresholds and descriptions for each level are presented in Table S1.

Table S1. Quartile-based classification of seismic density levels

Level	Range	Description
I	$[-4.5,\ Q1)$	Low seismic activity
II	$[Q1,\ Q2)$	Moderate seismic activity
III	$[Q2,\ Q3)$	High seismic activity
IV	$[Q3,\ \max]$	Extremely high seismic activity

Remark: Quartile-based classification of seismic density levels

$\max = -0.13;\quad Q(1) = -2.41;$

$Q(2) = -3.21;\quad Q(3) = -3.95.$

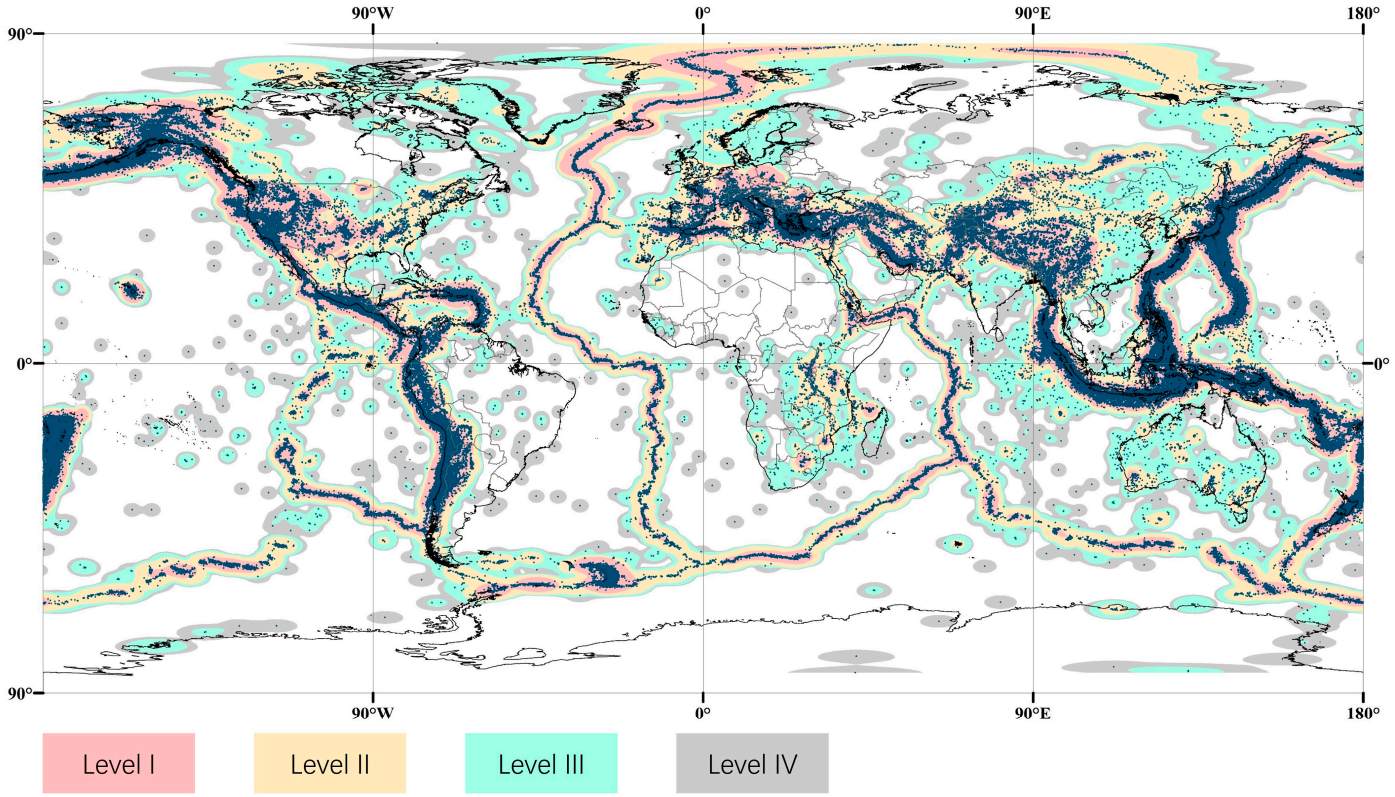


Figure S7 Quantification and Classification of Seismically Active Zones

The map illustrates the spatial density of seismic events recorded from 2005 to 2020. The global seismicity is stratified into four intensity levels based on event frequency: Level I (Pink) represents hyper-active zones (e.g., the Circum-Pacific Belt); Level II (Yellow) and Level III (Green) denote high to moderate activity transitions; and Level IV (Grey) indicates background low-seismicity regions. The dark blue points represent the epicenter distribution of the dataset.

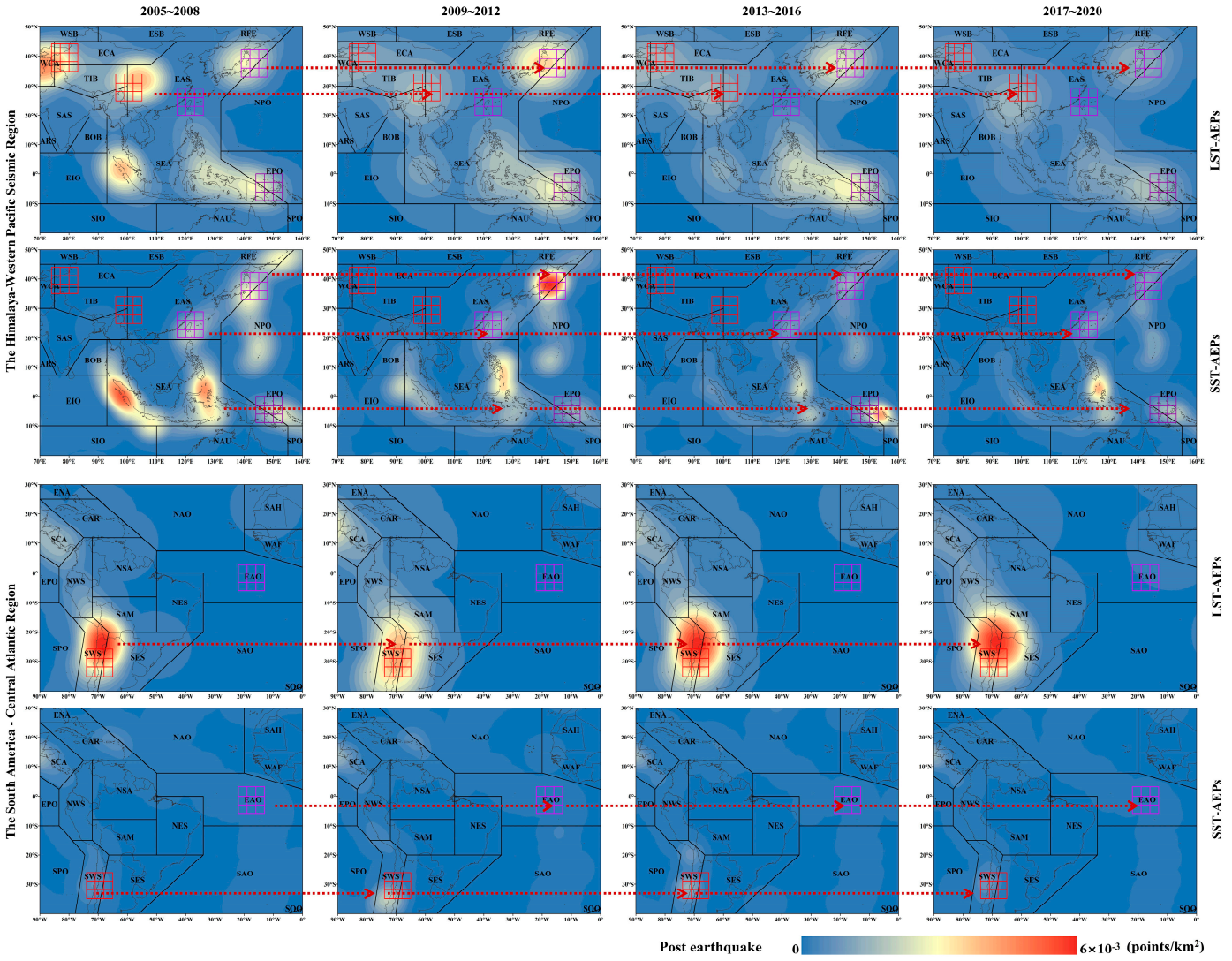


Figure S8 Spatiotemporal evolution of significant Post-earthquake Thermal Anomaly (AEP) density across two major seismic research zones from 2005 to 2020. The panels display the kernel density of AEPs derived from Land Surface Temperature (LST) and Sea Surface Temperature (SST) in four consecutive periods: 2005–2008, 2009–2012, 2013–2016, and 2017–2020. The Himalaya–Western Pacific Seismic Region. The distribution highlights the transition from continental (LST) to oceanic (SST) anomaly patterns. The South America – Central Atlantic Region, contrasting the Andean subduction zone (left, land-dominated) with the Mid-Atlantic Ridge (right, ocean-dominated). **Note:** This figure serves as supplementary evidence to validate the varying thermal inertia and coupling effects discussed in the main text (Section 4.3.1).

Figure S8 serves as supplementary validation for the proposed physical mechanisms. Mirroring the pre-seismic analysis, it illustrates the spatiotemporal evolution of anomalies in the post-seismic phase. The figure corroborates the distinct thermodynamic behaviors dictated by the regional environment: specifically, it highlights the "diffusion weakening" trend on land (due to low thermal inertia and rapid dissipation) versus the "diffusion enhancement" or persistence in oceanic regions. This consistent contrast between pre- and post-seismic phases reinforces the validity of the Lithosphere-Ocean-Atmosphere Coupling (LOAC) framework presented in the discussion.

S.1.5 Spatiotemporal evolution of significant Post-earthquake Thermal Anomaly (AEP)

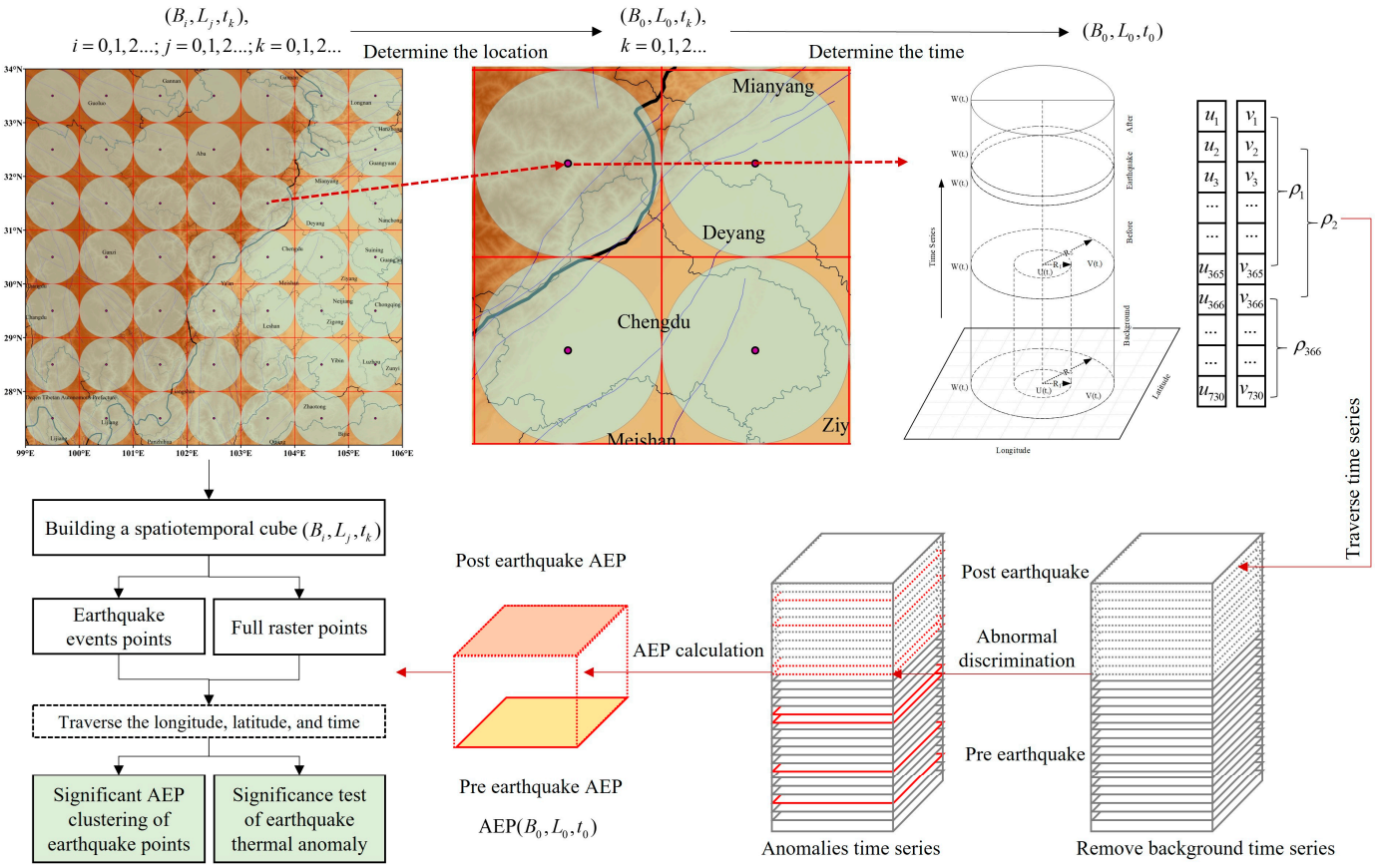


Figure S9 Flowchart for Thermal Anomaly Detection, AEP Calculation, and Significance Testing

The workflow comprises three stages: (1) Data Construction: Transforming raw remote sensing data into a standardized spatiotemporal cube (B_i, L_j, t_k) through spatial gridding and temporal alignment. (2) Anomaly Extraction: Traversing the time series to extract background, pre-seismic, and post-seismic vectors. A 'Remove background' process is applied to filter climatic noise, employing the detection algorithm from our proposed framework. (3) Quantification and Verification: Calculating the Anomaly Emphasis Proximity (AEP) indices for pre- and post-earthquake phases. This metric emphasizes the proximity or relevance of anomalies to seismic events. Finally, a significance test compares the AEP clustering of earthquake points against full raster points to validate the non-random nature of the detected thermal patterns.